 DOI: 10.31223/osf.io/9cafj

Spatially distributed chaos and turbulence in clouds

A. Bershadskii
ICAR, P.O. Box 31155, Jerusalem 91000, Israel
bershads@gmail.com

Spatially distributed chaos (turbulence) in the cumulus, stratocumulus, stratiform, cirrus and cirrus mammatus clouds have been studied using results of direct numerical simulations and measurements in the cloudy atmosphere. It is shown that in the considered cases the second order moment of helicity distribution (the Levich-Tsinober invariant) dominates the kinetic energy spectra.

I. INRODUCTION

The climate predictions and weather forecasting are heavily dependent on the modelling of the cloud formation under turbulent conditions. Therefore, a vast range of scales should be taken into account - from the cloud microphysical processes to the macroscopic turbulent motions. Both these non-linearly interacting components are poorly understood. The difficulty to conduct measurements of the microphysical properties of the real clouds formation under turbulent conditions (see, for instance, Ref. [1] and references therein) makes the problem formidable. Therefore, the recent direct numerical simulations (see, for instance, Refs. [2],[3], [4] and references therein) trying to take into account the maximum possible variance of the key microscopic and macroscopic processes (collision-coalescence of droplets, condensation-evaporation, the cooling related to the updraft motion inside the cumulus clouds, Reynolds number dependent drag, supersaturation, longwave radiative cooling etc.) in the buoyant turbulent environment are rather important.

In present paper results of the direct numerical simulations have been used in order to develop a comprehensive distributed chaos approach to the hydrodynamic aspects of the problem and are compared to atmospheric measurements.

In the Section II of the paper appearance of the temporally distributed chaos from the deterministic one is studied and compared with results of a direct numerical simulation of the Rayleigh-Bénard thermal convection. In the Section III the spatially distributed chaos in the Rayleigh-Bénard thermal convection has been studied and compared with results of direct numerical simulations. In the Section IV the buoyancy-helical distributed chaos have been introduced, studied and compared with the results of measurements in atmospheric boundary layer during a morning transition from the stable to adiabatic mixed-layer convective conditions. In the Sections V-VIII the buoyancy-helical distributed chaos has been studied in the cumulus, stratocumulus, stratiform, cirrus and cirrus mammatus clouds using results of direct numerical simulations and measurements in cloudy atmosphere.

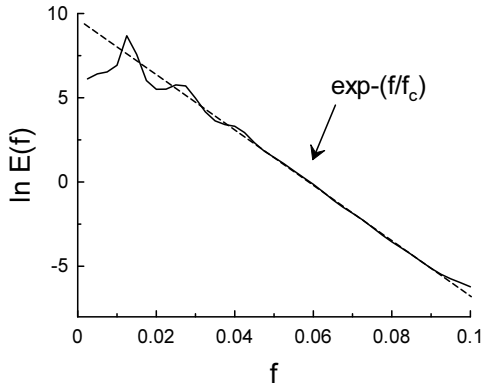

FIG. 1: Logarithm of power spectrum for z-component of the Eq. (1) against frequency f. The dashed straight line corresponds to Eq. (2).

II. FROM DETERMINISTIC TO DISTRIBUTED CHAOS

The deterministic chaos in the thermal convection was discovered by E.N. Lorenz [5] in a simplified model of the Rayleigh-Bénard convection

$$\frac{dx}{dt} = \sigma(y - x), \quad \frac{dy}{dt} = rx - y - xz, \quad \frac{dz}{dt} = xy - bz \quad (1)$$

The Rayleigh-Bénard convection is a thermal convection in a layer of fluid, cooled from above and heated from below. The parameters $b = 8/3$, $r = 28.0$, $\sigma = 10.0$, for instance, provide a chaotic solution. Fig. 1 shows power spectrum of z-component (in the semi-logarithmic scales). The spectrum was computed using the maximum entropy method, which provides an optimal resolution for comparatively short data sets [6]. The dashed straight line corresponds to the exponential spectrum

$$E(f) \propto \exp -(f/f_c) \quad (2)$$

where $f_c = const$ is some characteristic frequency. It is now well known that the exponential spectrum Eq. (2) is a typical spectrum for the deterministic chaos [6]- [10].

The Boussinesq approximation for the buoyancy-driven flows is (see, for instance, Ref. [11])

$$\frac{\partial \mathbf{u}}{\partial t} + (\mathbf{u}\cdot\nabla)\mathbf{u} = -\frac{\nabla p}{\rho_0} + \sigma g\theta \mathbf{e}_z + \nu\nabla^2\mathbf{u} \qquad (3)$$

$$\frac{\partial \theta}{\partial t} + (\mathbf{u}\cdot\nabla)\theta = S\frac{\Delta}{H}e_z u_z + \kappa\nabla^2\theta, \qquad (4)$$

$$\nabla\cdot\mathbf{u} = \mathbf{0} \qquad (5)$$

here p and θ are the pressure and temperature fluctuation fields ($\theta = T - T_0(z)$ with $T_0(z)$ as a conduction-state profile), $\mathbf{u}$ is the velocity field, $\mathbf{e}_z$ is the vertical unit vector, the vertical distance between the two layers is H and the temperature difference between them is Δ (in the case of the Rayleigh-Bénard convection the H is distance between the bottom and top plates), ρ_0 is the mean density of the fluid, ν is the viscosity and κ is the thermal diffusivity, the gravity acceleration is g and the thermal expansion coefficient is σ. For the unstably stratified flows (Rayleigh-Bénard convection) $S = +1$ whereas for the stably stratified flows $S = -1$.

In a direct numerical simulation of the Rayleigh-Bénard convection Eqs. (3-5), reported in Ref. [12], dynamics of a global characteristic - normalized heat current through the fluid layer $N(t)$ (the Nusselt number) at constant temperature of the top and bottom surfaces of a cylindrical domain, was studied at the onset of the thermal convection at Prandtl number $Pr = \nu/\kappa = 0.78$ and aspect ratio $\Gamma = 4.72$.

Figure 2 shows (in the log-log scales) a broadband windowed power spectrum of the $N(t)$ fluctuations obtained at $\delta = (Ra - Ra_c)/Ra_c = 0.614$, where Ra_c is the Rayleigh number at the convective threshold ($Ra = \sigma g \Delta H^3/\nu\kappa$). The spectral data were taken from Fig. 3 of the Ref. [12]. Observations performed in the Ref. [12] indicate that the spectrum shown in the Fig. 2 is dominated mainly by the nucleation of dislocation pairs.

The dashed curve in the Fig. 2 indicates the exponential spectrum Eq. (2) (position of the characteristic scale f_c is shown in the Fig. 2 by a dotted arrow). As it was already mentioned above such spectrum is an usual characteristic of smooth bounded deterministic dynamics.

With increase of the parameter δ the convection dynamics becomes more and more complicated and at the value $\delta \simeq 3$ time-series of the $N(t)$ fluctuations are already random-like (the dynamics in this case is dominated mainly by the the roll pinch-off events [12]). In order to understand this transition one should take into account that with the increase of δ the parameter f_c in the Eq. (2) becomes fluctuating and one should use an ensemble average over this fluctuating parameter (with

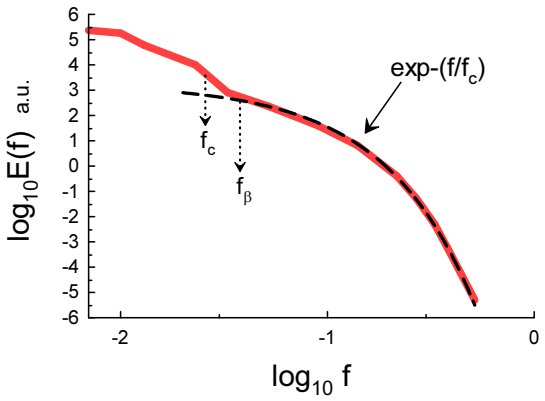

FIG. 2: Windowed power spectrum of the $N(t)$ fluctuations at $\delta = 0.614$.

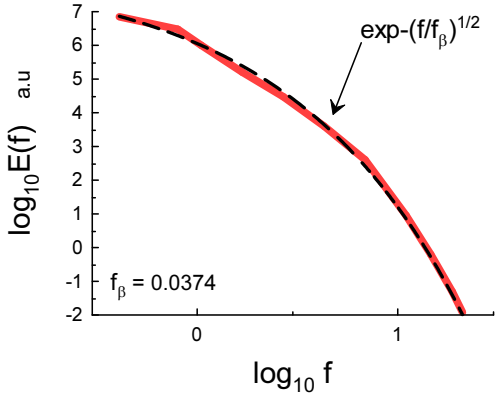

FIG. 3: Windowed power spectrum of the $N(t)$ fluctuations at $\delta = 3$.

certain distribution $P(f_c)$) to compute the power spectrum

$$E(f) = \int P(f_c)\ \exp -(f/f_c)\ df_c \qquad (6)$$

To find $P(f_c)$ let us recall that despite the thermal convection is not an Hamiltonian system there is a possibility to introduce an effective action I_e for such systems in the case of chaotic/stochastic dynamics (see Ref. [13] and references therein). The basic dynamic relationship involving the action is

$$u_c \propto I_e^{1/2} f_c^{1/2} \qquad (7)$$

where u_c is a characteristic velocity and I_e can be considered as an adiabatic invariant [14]. Providing Gaussian (normal) distribution of the characteristic velocity (see, for instance, Ref. [15]) we obtain

$$P(f_c) \propto f_c^{-1/2} \exp -(f_c/4f_\beta) \qquad (8)$$

where f_β = constant.

Substitution of the Eq. (8) into Eq. (6) results in

$$E(f) \propto \exp -(f/f_\beta)^{1/2} \tag{9}$$

Figure 3 shows a windowed power spectrum of the $N(t)$ fluctuations obtained at $\delta = 3$. The spectral data were taken from Fig. 3 of the Ref. [12]. The dashed curve in the Fig. 3 indicates the stretched exponential spectrum Eq. (9). It follows from comparison of the Figs. 2 and 3 that the stretched exponential power spectrum in the Fig. 3 is tuned to the low-frequency edge of the exponential spectrum shown in Fig. 2 - f_β (the second dotted arrow in the Fig. 2). It is natural if the distributed chaos at $\delta = 3$ is a result of the development of the deterministic chaos at $\delta = 0.614$.

III. SPATIALLY DISTRIBUTED CHAOS

The exponential power spectra are typical for deterministic chaos (or for onset of turbulence) not only in the frequency domain but for the wavenumber domain as well (see, for instance Refs. [7],[16] and references therein)

$$E(k) \propto \exp(-k/k_c) \tag{10}$$

With transition to turbulence, analogously to the temporal description, fluctuations of the characteristic wavenumber k_c can be taken into account by the ensemble averaging

$$E(k) \propto \int_0^\infty P(k_c) \exp -(k/k_c) dk_c \propto \exp -(k/k_\beta)^\beta \tag{11}$$

where the stretched exponential in the right-hand side of the Eq. (11) is a generalization of the Eq. (9). In this case the probability distribution $P(k_c)$ can be estimated for large k_c from the Eq. (11) [17]

$$P(k_c) \propto k_c^{-1+\beta/[2(1-\beta)]} \exp(-\gamma k_c^{\beta/(1-\beta)}) \tag{12}$$

where γ is a constant.

The spatial (wavenumber) version of the relationship Eq. (7) is

$$u_c \propto I_e k_c \tag{13}$$

Let us consider a general scaling

$$u_c \propto k_c^\alpha \tag{14}$$

If u_c has Gaussian distribution (with zero mean) [15] a relationship between α and β

$$\beta = \frac{2\alpha}{1+2\alpha} \tag{15}$$

follows immediately from the Eqs. (12) and (14).

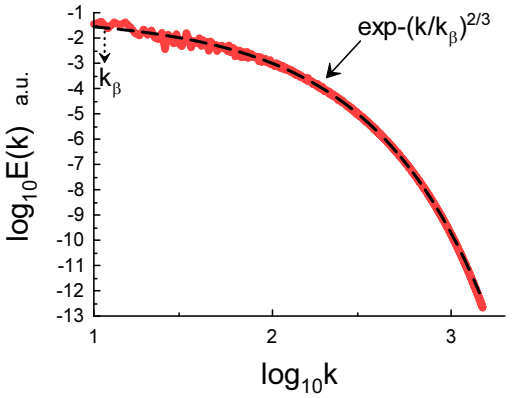

FIG. 4: Spatial kinetic energy spectrum at $Pr = 1$ and $Ra = 10^8$.

Then for the particular case Eq. (13) $\alpha = 1$, hence $\beta = 2/3$, i.e.

$$E(k) \propto \exp -(k/k_\beta)^{2/3}. \tag{16}$$

In recent Ref. [18] results of a direct numerical simulations of the Rayleigh-Bénard convection at $Ra = 10^8$ (still a moderate value) and the Prandtl number $Pr = \nu/\kappa = 1$ were reported. The free-slip boundary conditions for the velocity field and conducting boundary conditions for the temperature field were used at the top and bottom horizontal plates, whereas at the side walls of the computational domain the periodic boundary conditions were used and random initial condition were applied.

Figure 4 shows spatial kinetic energy spectrum obtained in this DNS. The dashed curve is drawn in order to indicate the stretched exponential spectrum Eq. (16) and the dotted arrow indicates k_β.

IV. HELICAL DISTRIBUTED CHAOS

Let us consider equation for mean helicity $h = \mathbf{u} \cdot \boldsymbol{\omega}$ (here the vorticity $\boldsymbol{\omega} = \nabla \times \mathbf{u}$) corresponding to the Eq. (3) with $\nu = 0$

$$\frac{d\langle h \rangle}{dt} = 2\sigma g e_z \langle \omega_z \theta \rangle \tag{17}$$

where $\langle ... \rangle$ denotes an average over volume.

It follows from the Eq. (17) that the helicity generally is not an ideal invariant of the Rayleigh-Bénard convection. However, one can expect that the correlation $\langle \omega_z \theta \rangle$ being considerable at large scales (on the coherent structures) is quickly decreased in the chaotic/turbulent motion when the spatial scales become smaller. Therefore, the second order moment of the helicity distribution (the Levich-Tsinober invariant of the Euler equation [19]) can be still considered as an ideal invariant of the Rayleigh-Bénard convection. Indeed, let us divide the volume of

motion into the cells V_j subject to the boundary conditions $\boldsymbol{\omega}\cdot\mathbf{n}=0$ on the bounding surfaces of the cells - S_j, moving with the fluid [19],[20]. Then for the sells (where the spatial scales are small enough) the helicity, averaged over the cell, can be approximately considered as an ideal invariant. The second order moment can be defined as [20]

$$I=\lim_{V\to\infty}\frac{1}{V}\sum_j H_j^2 \tag{18}$$

where

$$H_j=\int_{V_j} h(\mathbf{r},t)\,d\mathbf{r}. \tag{19}$$

For a strong convection (e.g. for large Ra) one can expect that the cells with the approximately conserved H_j^2 provide the main contribution to the sum in the Eq. (18) (cf. Ref. [21]) then the second order moment I is approximately an ideal invariant of the Rayleigh-Bénard convection.

For an inertial range of scales the ideal invariant I can be considered as an adiabatic invariant even for the viscous Eq. (3) and, therefore, can replace the I_e in the Eq. (13)

$$u_c\propto I^{1/4}k_c^{1/4} \tag{20}$$

from the dimensional considerations (i.e. $\alpha=1/4$). Then, it follows from the Eq. (15) that $\beta=1/3$, i.e.

$$E(k)\propto\exp-(k/k_\beta)^{1/3} \tag{21}$$

for the helically dominated convection. Of course, as for the I_e dominated convection, this consideration is valid for both the stable and unstable stratification.

Figure 5 shows power spectrum of the longitudinal velocity fluctuations measured at the altitude 100 m in the atmospheric boundary layer during a morning transition from the stable to adiabatic mixed-layer convective conditions (the spectral data were taken from Fig. 3a of the Ref. [22]). The high Reynolds number data were obtained with a small unmanned aerial system. The dashed curve is drawn in the Fig. 5 in order to indicate the stretched exponential spectrum Eq. (21) and the dotted arrow indicates position of k_β.

V. DISTRIBUTED CHAOS IN CUMULUS CLOUDS

In cumulus clouds the buoyancy-driven thermal convection is complicated by collision-coalescence of droplets with hydrodynamic interaction and Reynolds number dependent drag. Nonlinear interaction between turbulent mixing and the condensation-evaporation process

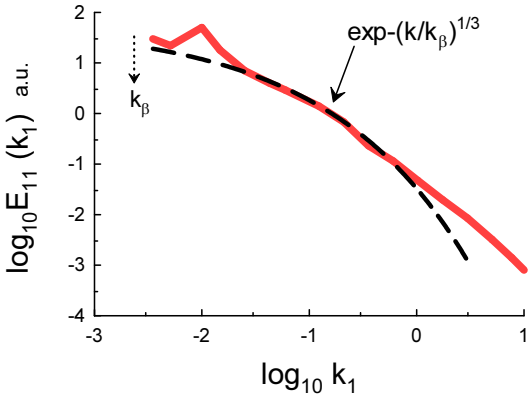

FIG. 5: Power spectrum of the longitudinal velocity fluctuations measured at the altitude 100 m in the high Reynolds number atmospheric boundary layer during a morning transition from the stable to adiabatic mixed-layer convective conditions.

(in presence of large numbers of droplets) should also strongly affect the convection and evolution of cloud droplets.

There exist many models for description of this complex system. For instance, it was suggested (see recent Ref. [2] and references therein) to consider a small air parcel (a cubic box with volume L^3) ascending inside the core region of a (maritime) cumulus cloud. In the sufficiently small parcel the fluctuating quantities can be considered as statistically homogeneous and the periodic boundary conditions in all three directions can be used. One have to consider corresponding equations describing dynamics of the parcel, flow and droplets.

To describe dynamics of the parcel one can use equations

$$\frac{\langle d\mathcal{H}(t)\rangle}{dt}=\langle W(t)\rangle\quad\frac{d\langle W(t)\rangle}{dt}=\langle B(t)\rangle \tag{22,23}$$

where $B(t)$ is a buoyancy force acting on the parcel, $W(t)$ and $\mathcal{H}(t)$ are corresponding updraft (vertical) velocity and altitude associated with the parcel.

To describe the flow velocity field $\mathbf{u}$, temperature θ and water vapor mixing ratio q one can use the Boussinesq approximation

$$\frac{\partial\mathbf{u}}{\partial t}+(\mathbf{u}\cdot\nabla)\mathbf{u}=-\frac{\nabla p}{\rho_0}+(B-\langle B(t)\rangle)\mathbf{e}_z+\nu\nabla^2\mathbf{u}+\mathbf{f} \tag{24}$$

$$\frac{\partial\theta}{\partial t}+(\mathbf{u}\cdot\nabla)\theta=-\Gamma u_z+\frac{L_v}{c_p}(C_d-\langle C_d\rangle)+\kappa\nabla^2\theta, \tag{25}$$

$$\frac{\partial q}{\partial t}+(\mathbf{u}\cdot\nabla)q=-(C_d-\langle C_d\rangle)+\kappa_q\nabla^2 q, \tag{26}$$

$$\nabla\cdot\mathbf{u}=\mathbf{0} \tag{27}$$

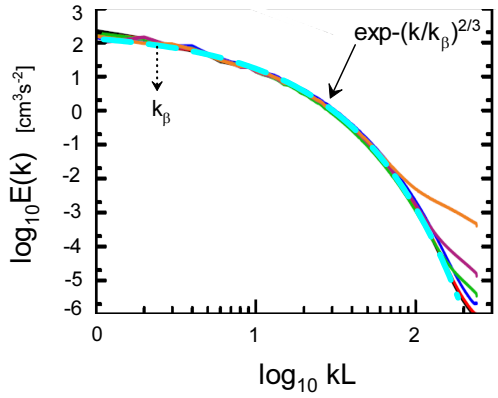

FIG. 6: Kinetic energy spectrum for $Re_\lambda = 104$.

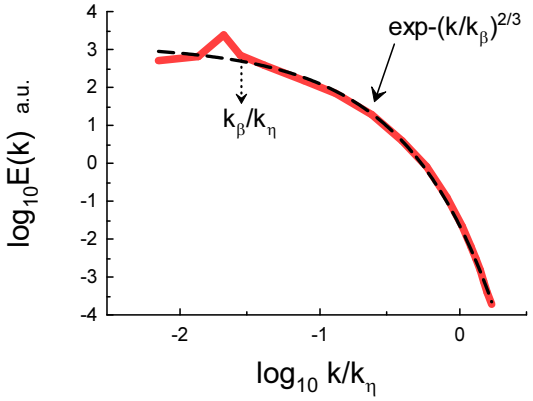

FIG. 8: Time-averaged kinetic energy spectrum for $Re_\lambda = 130$.

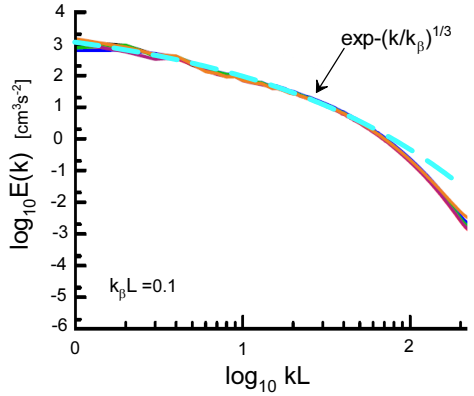

FIG. 7: Kinetic energy spectrum for $Re_\lambda = 167$.

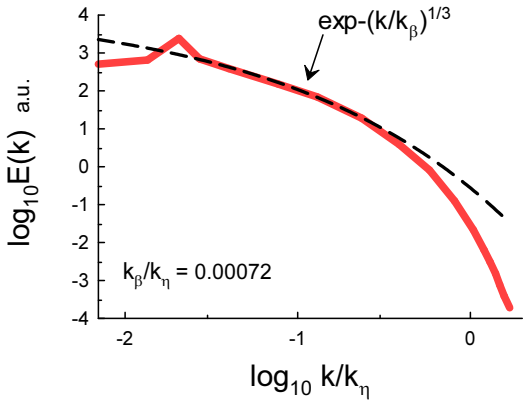

FIG. 9: The same as in the Fig. 8 but with the helically fitted (cf. Eq. (21)) inertial subrange.

in the local coordinate system associated with the parcel. In these equations $\mathbf{f}$ is an external (random) force, Γ represents the cooling effect related to the ascending motion of the parcel, C_d represents latent mass exchange through condensation in the Eq. (26) and heat release in the Eq. (25) (see for more details the Ref. [2]).

For the system Eqs. (24-27) the generalized action I_e and second order moment of helicity I are still adiabatic invariants for the inertial range of scales. Let us show this for the second order moment of helicity I.

The equation of the mean helicity for the ideal case ($\nu = 0$) is

$$\frac{d\langle h\rangle}{dt} = 2\langle \boldsymbol{\omega}\cdot\mathbf{F}\rangle \tag{28}$$

$$\mathbf{F} = (B - \langle B\rangle)\mathbf{e}_z + \mathbf{f} \tag{29}$$

(cf. Eq. (17)). If the correlation $\langle \boldsymbol{\omega}\cdot\mathbf{F}\rangle$ is negligible or it is not negligible for the large scales only then the consideration of the Section IV can be readily generalized for the Eq. (28) and the second order moment of helicity I is an adiabatic invariant for the inertial range of scales (in the former case it is an adiabatic invariant for the large scales as well). A direct numerical simulation with the above described model was performed in the Ref. [2] and figure 6 shows the kinetic energy spectrum obtained in this simulation for the Taylor-Reynolds number [15] $Re_\lambda = 104$ (the specral data were taken from Fig. 7 of the Ref. [2]). Different colors correspond to different times of the system's evolution: from $t = 10s$ (black) to $t = 600s$ (orange). The dashed curve indicates correspondence to the Eq. (16) (the action invariant I_e dominated distributed chaos).

Figure 7 shows the kinetic energy spectrum obtained in this simulation for the Taylor-Reynolds number $Re_\lambda =$

167 (the specral data were taken from Fig. 7 of the Ref. [2]). Different colors correspond to different times of the system's evolution: from the $t = 10s$ (black) to the $t = 600s$ (orange). The dashed curve indicates correspondence to the Eq. (21) (the helically dominated distributed chaos).

VI. STRATIFORM AND STRATOCUMULUS CLOUDS - DIRECT NUMERICAL SIMULATIONS

In the stratiform clouds the updraft velocity of the parcel is about zero [23],[24]. This results, in particular, in absence of the related cooling effect. Therefore, the condensational growth of the cloud droplets is mainly driven by supersaturation fluctuations (see, for instance, a recent Ref. [3] and references therein).

In the Ref. [3] a direct numerical simulation of a model corresponding to the stratiform clouds was performed with especial attention to the phenomenon of the cloud-droplet growth due to supersaturation fluctuations affected by turbulence (see the Ref. [3] for more detail). Figure 8 shows a time-averaged kinetic energy spectrum obtained in this simulation for $Re_\lambda = 130$ (the spectral data were taken from Fig. 1a of the Ref. [3]). The wavenumber is normalized by the Kolmogorov wavenumber $k_\eta = 2\pi/\eta$, where $\eta = (\langle\varepsilon\rangle/\nu^3)^{-1/4}$ is the Kolmogorov (dissipative) scale and $\langle\varepsilon\rangle$ is the mean dissipation rate due to viscosity [15]. The dashed curve indicates correspondence to the Eq. (16) (the action invariant I_e dominated distributed chaos).

Figure 9 shows the same spectral data but with the dashed curve indicating the helically dominated distributed chaos Eq. (21). One can see that there already exists an inertial subrange with the helically dominated distributed chaos, and one can expect that this subrange will be increased with Re_λ (cf. Figs. 6 and 7).

In the Ref. [4] results of a direct numerical simulation of stratocumulus cloud-top turbulence were reported (see for more details of the setting and simulations in the Refs. [25],[26]). In the cloud-top region longwave radiative cooling results in convective instability, that is a major source of chaotic (turbulet) motion in the cloud's region.

Figure 10 shows longitudinal spectrum of the horizontal velocity obtained in this simulation (the spectral data were taken from Fig. 4 of the Ref. [4], excluding the data for the upper part of cloud). Figure 11 shows corresponding transverse spectrum and again dashed curve indicates the helically dominated distributed chaos Eq. (21). Figure 12 shows longitudinal spectrum of the horizontal velocity obtained in this simulation for the upper part of cloud. The dashed curves in the Figs. 10-12 indicate the helically dominated distributed chaos Eq. (21).

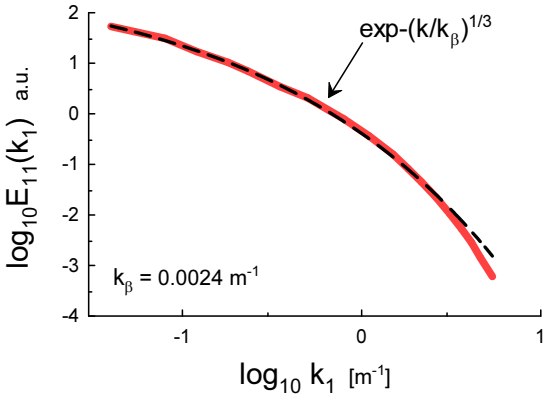

FIG. 10: Longitudinal spectrum of the horizontal velocity.

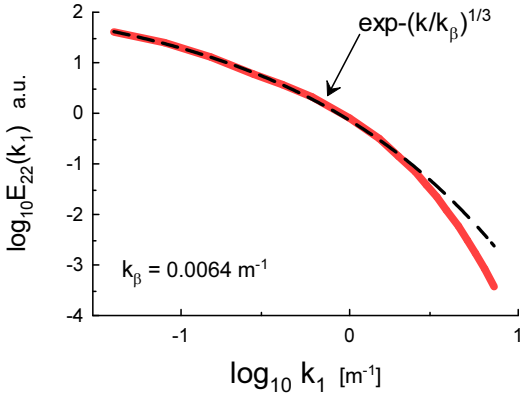

FIG. 11: Transverse spectrum of the horizontal velocity.

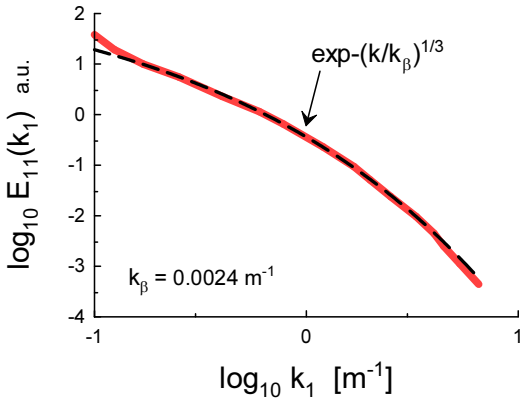

FIG. 12: Longitudinal spectrum of the horizontal velocity for upper part of cloud.

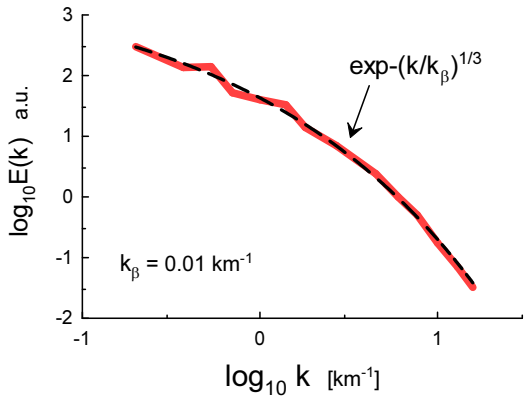

FIG. 13: 1D power spectrum of the radiance in the North-South direction (DF).

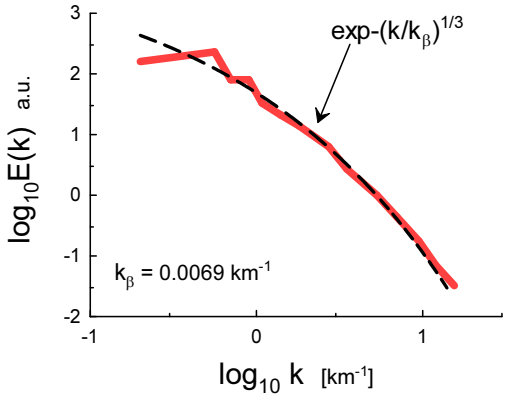

FIG. 14: 1D power spectrum of the radiance in the North-South direction (DA).

VII. STRATOCUMULUS CLOUDS - RADIOMETRIC MEASUREMENTS

A. Over land

The results of radiometric measurements made by the airborne Multiangle Imaging Spectro-Radiometer (AirMISR), on the NASA ER-2 high-altitude ($\sim$ 20 km) aircraft, were reported in Ref. [27]. The measurements were made for the blue channel radiance ($\lambda = 0.443$ μm) over continental single-layer low stratocumulus clouds. Therefore, one can expect that the radiance fluctuations were produced mainly by the velocity field at the top of the clouds.

Figure 13 shows 1D power spectrum of the radiance in the North-South direction: zenith angle 70.5^o and scattering angle 140.8^o (the spectral data were taken from Fig. 7-DF of the Ref. [27]). Figure 14 shows 1D spectrum of the radiance in the North-South direction: zenith angle 70.5^o and scattering angle 72.3^o (the spectral data were taken from Fig. 7-DA of the Ref. [27]). The DF and DA camera's view angles are the most oblique ones and for them the cloud gaps close about completely.

Figure 15 shows 1D spectrum of the radiance in the East–West direction (the spectral data were taken from Fig. 8-DF of the Ref. [27]). Figure 16 shows 1D spectrum of the radiance in the the East-West direction direction (the spectral data were taken from Fig. 8-DA of the Ref. [27]). The dashed curves in the Figs. 13-16 indicate the helically dominated distributed chaos Eq. (21).

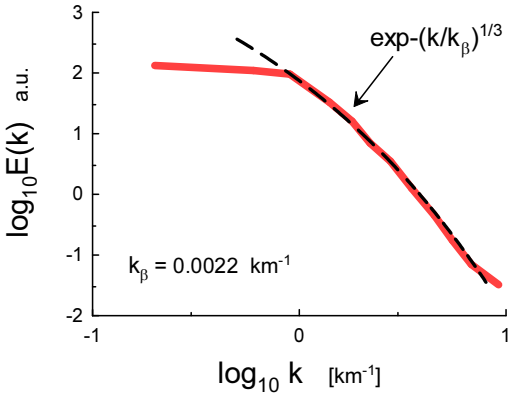

FIG. 15: 1D power spectrum of the radiance in the East-West direction (DF).

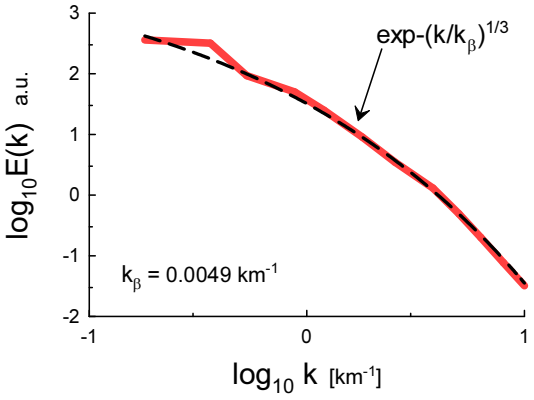

FIG. 16: 1D power spectrum of the radiance in the East-West direction (DA).

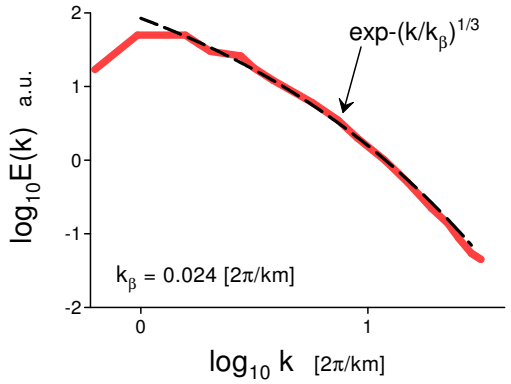

FIG. 17: Power spectrum of the cloud top reflectance over the marine stratocumulus clouds.

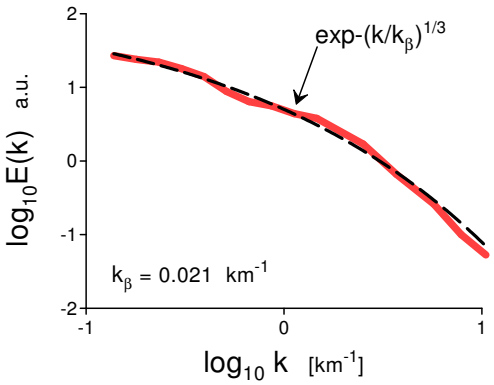

FIG. 19: Power spectrum of the Doppler velocity (cirrus mammatus clouds).

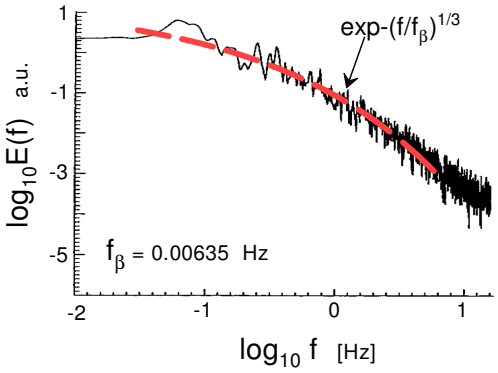

FIG. 18: Power spectrum of the vertical velocity fluctuations (cirrus clouds).

B. Over ocean

The results of radiometric measurements made by the airborne Multispectral Cloud Radiometr (MCR), on the NASA ER-2 high-altitude ($\sim$ 20 km) aircraft, were reported in Ref. [28]. The measurements were made for the visible channel radiance ($\lambda = 0.754$ μm) over the marine stratocumulus clouds (scanning was made in the direction perpendicular to the line of flight).

Figure 17 shows the spectrum of the cloud top reflectance. The spectral data were taken from Fig. 9 of the Ref. [28]. The dashed curve in the Fig. 17 indicates the helical distributed chaos Eq. (21).

VIII. CIRRUS AND CIRRUS MAMMATUS CLOUDS

Cirrus clouds are composed mainly of ice and are covering extensive areas in the upper troposphere. Therefore, they play the important role in the earth's radiation budget. The cirrus cloud structure and their optical properties significantly depend on the inner turbulent processes.

In the paper Ref. [29] results of aircraft measurements made in relatively thick frontal cirrus clouds during the daytime were reported.

Figure 18 shows power spectrum of the vertical velocity fluctuations measured at the straight horizontal flights of the aircraft over the region of Wick in Scotland at a height of 8.9 km. This is a frequency spectrum (the spectral data were taken from Fig. 7a of the Ref. [29]). However, the frequency spectrum can be readily converted into the wavenumber spectrum using the Taylor hypothesis [15] with $f = U_0\ k/2\pi$, where k is horizontal wavenumber and U_0 is the aircraft velocity. The dashed curve indicates the helically dominated distributed chaos Eq. (21).

Mammata are protuberances on the undersides of the clouds. The observations show [30] that cirrus mammata belong to the transition zone from dry air to the cloudy (moist) layers. In the paper Ref. [30] the Doppler velocity data inferred from the cirrus cloud-base region (a 10-yr subset of high-cloud radar data) were used to compute the power spectra of the Doppler velocity in the cirrus mammatus clouds.

Figure 19 shows power spectrum corresponding to the altitude 7.9 km (the spectral data were taken from the Fig. 7a of the Ref. [30]). The dashed curve indicates the helically dominated distributed chaos Eq. (21).

IX. ACKNOWLEDGEMENT

I thank E. Levich for stimulating discussions, and R. Samuel and M.K. Verma for sharing their data.

[1] H. Siebert, S. Gerashchenko, A. Gylfason, K, Lehmann, L,R. Collins, R.A. Shaw and Z. Warhaft, Atmos. Res., **97** 436 (2010).
[2] I. Saito and T. Gotoh, New J. Phys., **20** 023001 (2018).
[3] X-Y. Li, G. Svensson, A. Brandenburg and N.E.L. Haugen, Atmos. Chem. Phys., **19**, 639 (2019).
[4] E.O. Akinlabi, M. Waclawczyk, J. Mellado, and S. Malinowski, J. Atmos. Sci., **76**, 1471 (2019)
[5] E.N. Lorenz, J. Atmos. Sci., **20**, 130 (1963).
[6] N. Ohtomo, K. Tokiwano, Y. Tanaka et. al., J. Phys. Soc. Jpn. **64** 1104 (1995).
[7] J. E. Maggs and G. J. Morales, Phys. Rev. Lett. **107**, 185003 (2011); Phys. Rev. E **86**, 015401(R) (2012); Plasma Phys. Control. Fusion **54** 124041 (2012)
[8] D.E. Sigeti, Phys. Rev. E, **52**, 2443 (1995).
[9] J. D. Farmer, Physica D, **4**, 366 (1982).
[10] U. Frisch and R. Morf, Phys. Rev., **23**, 2673 (1981).
[11] A. Kumar, A.G. Chatterjee and M.K. Verma, Phys. Rev. E, **90**, 023016 (2014)
[12] M.R. Paul, M.C. Cross, P.F. Fischer, and H.S. Greenside, Phys. Rev. Lett., **87**, 154501 (2001).
[13] G.L. Eyink, Physica D, **239**, 1236 (2010).
[14] R.Z. Sagdeev, D.A. Usikov, G.M. Zaslavsky, Nonlinear Physics: from the Pendulum to Turbulence and Chaos (Harwood, New York, 1988)
[15] A. S. Monin, A. M. Yaglom, Statistical Fluid Mechanics, Vol. II: Mechanics of Turbulence (Dover Pub. NY, 2007).
[16] S. Khurshid, D.A. Donzis, and K.R. Sreenivasan, Phys. Rev. Fluids, **3**, 082601(R) (2018).
[17] D.C. Johnston, Phys. Rev. B, **74**, 184430 (2006).
[18] S. Vashishtha, M.K. Verma and R. Samuel, Phys. Rev. E., **98**, 043109 (2018).
[19] E. Levich and A. Tsinober, Phys. Lett. A **93**, 293 (1983).
[20] H.K. Moffatt and A. Tsinober, Annu. Rev. Fluid Mech., **24**, 281 (1992).
[21] A. Bershadskii and A. Tsinober, Phys. Rev. E, **48**, 282 (1993).
[22] C.A. Canter and S.C.C. Bailey, Proc. of the "11th International Symposium on Turbulence and Shear Flow Phenomena" (2019). http://www.tsfp-conference.org/proceedings/2019/304.pdf
[23] J.G. Hudson and G. Svensson, J. Appl. Meteorol., **34**, 2655 (1995).
[24] A.V. Korolev, J. Atmos. Sci., **52**, 3620 (1995).
[25] J.P. Mellado, Annu. Rev. Fluid Mech., **49**, 145 (2017).
[26] B. Schulz and J.P. Mellado, J. Atmos. Sci., **75**, 3245 (2018).
[27] M. Ovtchinnikov and R.T. Marchand, Remote Sensing of Environment, **107**, 185 (2007).
[28] R. Boers, J.D Spinhirne and W.D. Hart, J. Applied Met., **27**, 797 (1988)
[29] S.A. Smith and P.R. Jonas, Annales Geophysicae EGU, **15** 1447 (1997)
[30] L. Wang and K. Sassen, J. Atmos. Sci., **63**, 712 (2006)